JACS
JOURNAL OF THE AMERICAN CHEMICAL SOCIETY
Article
Cite This: J. Am. Chem. Soc. 2018, 140, 18115−18123
pubs.acs.org/JACS

# Chemical Insights into PbSe−x%HgSe: High Power Factor and Improved Thermoelectric Performance by Alloying with Discordant Atoms

James M. Hodges,[†] Shiqiang Hao,[‡] Jann A. Grovogui,[‡] Xiaomi Zhang,[‡] Trevor P. Bailey,[§] Xiang Li,[∥] Zhehong Gan,[⊥] Yan-Yan Hu,[∥,⊥] Ctirad Uher,[§] Vinayak P. Dravid,[‡] Chris Wolverton,[‡] and Mercouri G. Kanatzidis*[,†]

[†]Department of Chemistry, Northwestern University, Evanston, Illinois 60208, United States
[‡]Department of Materials Science and Engineering, Northwestern University, Evanston, Illinois 60208, United States
[§]Department of Physics, University of Michigan, Ann Arbor, Michigan 48109, United States
[∥]Department of Chemistry and Biochemistry, Florida State University, Tallahassee, Florida 32306, United States
[⊥]National High Magnetic Field Laboratory, 1800 East Paul Dirac Drive, Tallahassee, Florida 32310, United States

Supporting Information

**ABSTRACT:** Thermoelectric generators can convert heat directly into usable electric power but suffer from low efficiencies and high costs, which have hindered wide-scale applications. Accordingly, an important goal in the field of thermoelectricity is to develop new high performance materials that are composed of more earth-abundant elements. The best systems for midtemperature power generation rely on heavily doped PbTe, but the Te in these materials is scarce in the Earth's crust. PbSe is emerging as a less expensive alternative to PbTe, although it displays inferior performance due to a considerably smaller power factor $S^2\sigma$, where $S$ is the Seebeck coefficient and $\sigma$ is electrical conductivity. Here, we present a new p-type PbSe system, $Pb_{0.98}Na_{0.02}Se-x\%HgSe$, which yields a very high power factor of ~20 $\mu W \cdot cm^{-1} \cdot K^{-2}$ at 963 K when $x = 2$, a 15% improvement over the best performing PbSe−x%MSe materials. The enhancement is attributed to a combination of high carrier mobility and the early onset of band convergence in the Hg-alloyed samples (~550 K), which results in a significant increase in the Seebeck coefficient. Interestingly, we find that the $Hg^{2+}$ cations sit at an off-centered position within the PbSe lattice, and we dub the displaced Hg atoms "discordant". DFT calculations indicate that this feature plays a role in lowering thermal conductivity, and we believe that this insight may inspire new design criteria for engineering high performance thermoelectric materials. The high power factor combined with a decrease in thermal conductivity gives a high figure of merit $ZT$ of 1.7 at 970 K, the highest value reported for p-type PbSe to date.

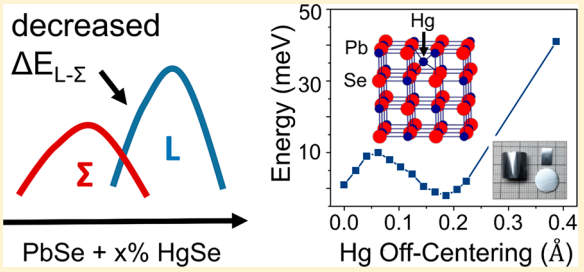


## INTRODUCTION

Global energy consumption is anticipated to double by midcentury, which could impose enormous environmental and socioeconomic challenges.[1] More than two-thirds of generated energy is lost as wasted heat, and accordingly, technologies that can capture and utilize such heat sources are expected to play an important role in the emerging sustainable energy portfolio.[2,3] Thermoelectric generators can convert heat directly into usable electric power and can be scaled to accommodate a wide variety of heat sources. Still, thermoelectric devices suffer from poor efficiencies and high manufacturing costs. Moving forward, an important goal in the field is to develop new materials that can facilitate high thermoelectric performance while also being composed of inexpensive, earth-abundant elements.

The maximum efficiency of a thermoelectric material is defined by the dimensionless figure of merit, $ZT = S^2\sigma/\kappa$, where $S$ is the Seebeck coefficient, $\sigma$ is the electrical conductivity, and $\kappa$ is the thermal conductivity. Thus, good thermoelectric materials must have high electrical conductivity and high thermopower ($S$) while also exhibiting low thermal conductivity. Since these are typically conflicting material properties, designing and optimizing thermoelectric systems are notoriously challenging. Historically, chalcogenides of the p-block metals (Bi, Pb, Sn, etc.) have been the most widely used materials for thermoelectrics due to their intrinsically low thermal conductivity, complex band structures, and chemical versatility.[4−8] PbTe is widely regarded as the best material system for midtemperature power generation (500−900 K),[9] but Te is among the rarest elements on Earth and very expensive, which may prove problematic for wide-scale heat recovery applications. PbSe is emerging as an attractive alternative because it shares many of the same features as

Received: October 13, 2018
Published: November 21, 2018






DOI: 10.1021/jacs.8b11050
J. Am. Chem. Soc. 2018, 140, 18115−18123

PbTe while also being composed of earth-abundant elements.[10] Moreover, PbSe has a higher melting point, is less brittle,[11] and, surprisingly, has lower intrinsic thermal conductivity than PbTe.[12] Heavily doped p-type PbSe has been predicted to have a figure of merit greater than 2.0 at high temperatures (p-type),[13] although the highest reported value is 1.6,[14] which indicates that further optimization is possible.

In the past decade there has been an influx of new successful strategies for optimizing thermoelectric materials. For example, nanostructuring and defect-engineering have yielded materials with extraordinary low thermal conductivity and record-breaking performance.[15−21] In fact, in many important systems, the thermal conductivity is now approaching the amorphous limit, which places a boundary on further progress. Accordingly, strategies that enhance the power factor ($S^2\sigma$) of thermoelectrics are expected to play an increasing role in future advances. It is well-known that large band degeneracy ($N_V$) can yield an enhancement in thermopower by increasing the density of states near the Fermi level.[22−27] In recent years, chemical alloying has emerged as a powerful tool for manipulating band structure to achieve greater $N_V$ and improved thermoelectric performance. For example, in p-type PbTe, isovalent alloying can be used to fine-tune the energy difference between the primary valence band ($N_v$ = 4) and the secondary valence band ($N_v$ = 12).[28,29] This provides control over the temperature at which the two bands converge to give maximum band degeneracy ($N_v$ = 16) and peak performance. Such strategies are far less explored in p-type PbSe, in large part due to the greater energy offset (~0.3 eV) between the primary and secondary valence bands in this material, which make it more difficult to converge.

Here, we present a new p-type PbSe system, $Pb_{0.98}Na_{0.02}Se-x\%HgSe$ ($x$ = 1−5), which exhibits an ultrahigh power factor of approximately 20 $\mu W \cdot cm^{-1} \cdot K^{-2}$ at 900 K when $x$ = 2. The augmented electronic properties are due to a substantial increase in the thermopower that begins around 550 K, which is not observed in the unalloyed $Pb_{0.98}Na_{0.02}Se$ samples. We attribute this enhancement to the early onset of band convergence, which is caused by a decrease in the energy offset between the valence bands located at the L-point (primary) and along the $\sum$-line (secondary) in the Brillouin zone (Figure 1). From a chemical perspective this is intuitive since the valence band edge in PbSe is dominated by the $6s^2$ electrons from $Pb^{2+}$, which are absent in $Hg^{2+}$ (Figure 1). Combined with a moderate decrease in thermal conductivity, the $Pb_{0.98}Na_{0.02}Se-2\%HgSe$ sample is found to have a maximum $ZT$ of approximately 1.7 at 970 K, which is the highest value reported for p-type PbSe.

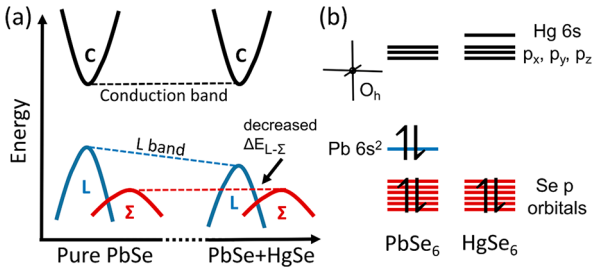


**Figure 1.** (a) Illustration of band diagram showing a decrease in the energy offset between the L-band and Σ-band with the addition of Hg into PbSe. (b) Molecular orbital scheme highlighting the absence of the $6s^2$ electrons in $Hg^{2+}$, which has the effect of lowering the energy of the L-band edge.

From a fundamental chemistry perspective, the $PbSe-x\%$ HgSe alloy is an intriguing material. PbSe is most stable in the rocksalt-type crystal structure (cubic, octahedral coordination) and has a narrow bandgap of approximately 0.27 eV. In contrast, HgSe adopts the zincblende-type structure (cubic, tetrahedral coordination) and is metallic. Surprisingly, we find that the bandgap of $PbSe-x\%HgSe$ alloy increases with the addition of HgSe, and we attribute this unexpected behavior to the unusual 6-fold coordination environment of $Hg^{2+}$ in the PbSe lattice. It is interesting to note that Hg is very rarely found with true octahedral coordination in either solid-state or molecular compounds,[30] which is attributed to relativistic effects.[31,32] This led us to speculate that Hg may sit at an off-centered position. Using $^{199}Hg$ and $^{77}Se$ NMR, we provide empirical evidence for an asymmetric coordination environment of $Hg^{2+}$ in the PbSe-HgSe pseudobinary alloy, which is supported by DFT calculations. We describe the off-centered Hg atoms as "discordant", since their intrinsic chemical character is out of harmony with the coordination requirements of the surrounding crystal matrix (e.g., tetrahedral for Hg vs octahedral for Pb). Such off-centering is being observed in a growing number of materials, including the case of $Ge^{2+}$ atoms in the n-type $PbSe-12\%GeSe$ system.[33] We discuss the influence this feature has on the charge and thermal transport of $PbSe-x\%HgSe$ and believe this may be an important, yet overlooked aspect in controlling the properties of lead chalcogenide semiconductors.

## EXPERIMENTAL SECTION

**Materials.** Lead wire (Pb, 99.999%, American Elements, USA), mercury metal (Hg, 99.999%, Sigma-Aldrich, USA), sodium chunk (Na, 99.999%, Sigma-Aldrich, USA), and selenium shot (Se, 99.999%, 5 N Plus, Canada) were all used as received.

**Synthesis of HgSe Precursor.** To synthesize the HgSe precursor, elemental Hg and Se in a 1:1 stoichiometric ratio (30 g total) were placed into a long fused-silica tube and flame-sealed at approximately $10^{-4}$ Torr. The sealed reaction tube was then placed into a vertically oriented tube furnace with the top end of the tube extending outside of the furnace. The samples were then heated to 823 K over 48 h and soaked at this temperature for 10 h, followed by cooling to room temperature in the furnace. Due to the high vapor pressure of HgSe, the final product condenses on the cold end of the tube that is outside of the furnace. *Caution: Hg, Se, and HgSe are toxic and have high vapor pressure at elevated temperatures that can result in explosions during the synthesis. Accordingly, great care should be taken when handling and synthesizing these materials and should only be carried out by trained personnel.*

**Synthesis of $Pb_{0.98-x}Na_{0.02}Hg_xSe$.** Ingots (15 g) of $Pb_{0.98-x}Na_{0.02}Hg_xSe$ ($x$ = 0.01, 0.02, 0.03, 0.04, 0.05) were synthesized by first placing the appropriate amount of Pb, Se, Na, and HgSe into carbon coated fused-silica tubes, which were then flame-sealed at approximately $10^{-4}$ Torr. The reaction tubes were then placed into a box furnace and heated to 773 K at a rate of 50 K/h and then soaked at this temperature for 5 h, in order to react the Se and minimize the chance of explosions at higher temperatures. The samples were then heated to 1473 K at a rate of 100 K/h and then allowed to react for 4 h. The samples were shaken gently after 3 h to ensure good mixing. To maximize the amount of Hg incorporated into the PbSe matrix, the samples were then water quenched. The $Pb_{1-x}Hg_xSe$ samples (2 g) used for bandgap measurements were synthesized using the same technique.

**Densification.** The $Pb_{0.98-x}Na_{0.02}Hg_xSe$ ingots were ground into fine powders using an agate mortar and pestle, and then passed through a 100 mesh sieve. The powders were then pressed into 12.7


DOI: 10.1021/jacs.8b11050
J. Am. Chem. Soc. 2018, 140, 18115−18123

mm pellets using a spark plasma sintering instrument (SPS, SPS-211LX, Fuji Electronic Industrial Co., Ltd.). The SPS was operated at 873 K under an axial pressure of 40 MPa for 10 min. The density of the pellets was calculated from their physical dimensions and masses and, in each case, exceeded 95% of the theoretical density.

**Optical Properties.** Fourier-Transform Infrared Spectroscopy (FTIR) was used to determine the optical bandgaps of the $Pb_{1-x}Hg_xSe$ ($x$ = 0.02, 0.04, 0.06, 0.08, 0.10) samples. Reflectance data was collected using a Nicolet 6700 IR spectrometer under a flow of nitrogen, and the data was then converted to absorbance using the Kubelka–Munk relationship ($f(R) = (1 - R^2)/2R = \alpha/S$, where $R$ is absolute reflectance, $\alpha$ is the absorption coefficient, and $S$ is the scattering coefficient).[34]

**$^{77}$Se and $^{199}$Hg NMR.** Both $^{77}$Se and $^{199}$Hg solid-state NMR experiments were performed using a Bruker 830 MHz DRX spectrometer and a 31 mm 19.6 T magnet. The NMR Larmor frequency is 158.90 MHz for $^{77}$Se and 150.35 MHz for $^{199}$Hg. A home-built magic-angle spinning probe was used under static sample conditions. Samples were packed into 3.2 mm thin-wall rotors with 36 $\mu$L sample volume. The Carr–Purcell–Meiboom–Gill (CPMG) pulse sequence was employed for enhancing sensitivity with multiple-echo signal acquisition.[35] The 90° pulse lengths were 2 $\mu$s for $^{77}$Se and 3 $\mu$s for $^{199}$Hg. The recycle delays were set to be 30 s for both $^{77}$Se and $^{199}$Hg NMR acquisitions. $^{199}$Hg and $^{77}$Se shifts were referenced to 0 ppm based on the frequency table[36] and the $^{17}$O frequency of $H_2O$ was calibrated externally prior to the measurement.

**Thermal Conductivity.** The thermal conductivity of the samples was determined using the laser flash diffusivity (LFA) method. Briefly, the diffusivity ($D$) of the SPS-processed $Pb_{0.98-x}Na_{0.02}Hg_xSe$ pellets (~6 mm × 6 mm × 2 mm) was measured as a function of temperature using a Netzsch LFA457 instrument. To minimize radiative heat loss, the samples were coated with graphite. Thermal conductivity was then calculated using the equation $\kappa_{total} = DC_pd$, where $d$ is density and $C_p$ is heat capacity. Density was determined using the dimensions and mass of the sample, and $C_p$ was estimated from the relationship $C_p = [0.17078 + (2.64876 \times 10^{-5}) \times T(K)]$ J·g$^{-1}$·K$^{-1}$.[37] The electronic contribution to the thermal conductivity was estimated using the Wiedemann-Franz relationship $\kappa_{elec} = \sigma LT$, where $\sigma$ is the electrical conductivity and $L$ is the Lorenz number. $L$ was calculated using the chemical potential, which was estimated from the Seebeck coefficients as described elsewhere.[33] The lattice contribution to the thermal conductivity ($\kappa_{latt}$) was calculated by subtracting $\kappa_{elec}$ from $\kappa_{total}$.

**Electron Microscopy.** To investigate the microstructure across multiple length scales, scanning electron microscopy (SEM) and scanning transmission electron microscopy (S/TEM) was performed on both the $Pb_{0.98}Na_{0.02}Se$-2%HgSe and PbSe-6%HgSe samples. Larger microstructural features were investigated using SEM because of the larger field of view, primarily through electron imaging, energy dispersive spectroscopy (EDS), and electron backscattered diffraction (EBSD). Samples were prepared for EBSD by grinding using 600, 800, and 1200 grit SiC grinding paper. Surface deformation was polished away on a grinding wheel with a polishing cloth using 1 $\mu$m, 0.1 $\mu$m diamond slurry, and finishing with 0.05 $\mu$m alumina slurry in a vibratory polisher. Simultaneous EDS and EBSD were then performed on the samples using an FEI Quanta 650 ESEM. EBSD maps were then cleaned using the AZtec software package offered by Oxford Instruments. The image cleaning corrected unindexed points from residual surface imperfections and did not fundamentally change the grain structure that was revealed using EBSD. The TEM specimen was prepared using conventional methods, which included dicing, grinding, and dimpling, followed by 4 keV Ar ion milling until hole formation and cleaned with 2 keV. Ar ion milling was performed with a Gatan precision ion polish system (PIPS). Conventional TEM imaging, STEM high angle annular dark field (HAADF) imaging, and EDS were carried out with a JEOL ARM300F GrandARM TEM operated under 300 kV and a Hitachi HD-2300A Dual EDS Cryo S/TEM.

**Hall Measurements.** The temperature-dependent Hall effect was measured using homemade AC 4-probe system with excitation fields of plus/minus 0.5 and 1.0 T. The homemade system employs an air-bore, helium-cooled superconducting magnet to generate the field in a high temperature oven that surrounds the Ar-filled sample probe. The carrier concentration was estimated using the equation $N_p = 1/eR_H$, where $e$ is the elemental charge and $R_H$ is the measured Hall coefficient. The Hall mobility ($\mu_H$) was determined using the relationship $\mu_H = \sigma R_H$, where $\sigma$ is the electrical conductivity obtained from the ULVAC instrument.

## RESULTS AND DISCUSSION

In order to understand how Hg-alloying affects the optical properties of PbSe and also determine the approximate solubility limit, undoped PbSe–$x$%HgSe samples were synthesized using the high-temperature methods described above, and the corresponding XRD are shown in Figure 2a.

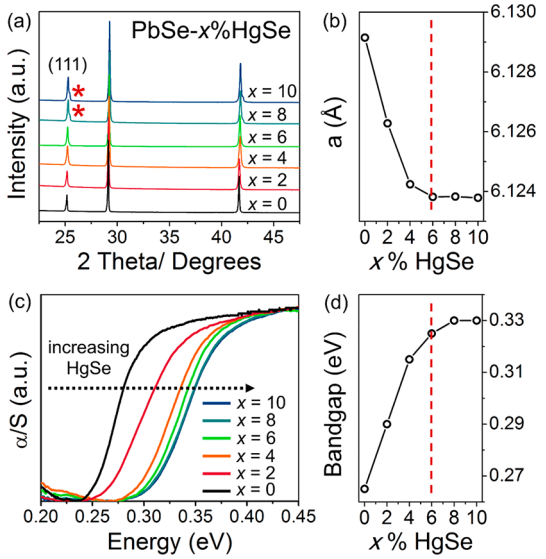


**Figure 2.** (a) Powder X-ray diffraction data and (b) refined lattice parameters for the PbSe–$x$%HgSe samples. A second set of peaks emerge as a shoulder at the (111) reflection of the 8% and 10% HgSe samples, which are denoted with an asterisk and are indexed to zincblende-type HgSe (Figure S1). (c) Absorption spectra for the PbSe-$x$%HgSe samples along with (d) calculated bandgaps. The red lines in parts b and d represent the approximate solubility limit.

Rocksalt-type PbSe can be indexed to each pattern and the lattice constants are found to decrease through 6% Hg, after which there is only a small change as shown in Figure 2b. The lattice contraction is expected since $Hg^{2+}$ has a smaller ionic radius (1.02 Å) than $Pb^{2+}$ (1.29 Å). A second set of peaks emerge in the 8% and 10% Hg samples, which can be indexed to zincblende-type HgSe and indicates that the maximum solubility was exceeded (Figure 2a, S1). Diffuse reflectance spectra were collected for each composition using FTIR and then converted to absorption using the Kebulka–Munk relationship, as is shown in Figure 2c. Clearly, there is a blueshift in the absorption edge with increasing Hg content, which appears to saturate at approximately 6% Hg. The bandgaps of the samples are found to increase from 0.27 ($x$ = 0) to 0.33 eV ($x$ = 6), after which there is only a minimal change (Figure 2c). SEM and EBSD were used to examine the chemical homogeneity and microstructure of the PbSe–6% HgSe sample, and the data is shown in Figure S2. We observe that Hg is well distributed throughout the PbSe matrix at the micron scale, while there are trace amounts of Se at the grain


DOI: 10.1021/jacs.8b11050
J. Am. Chem. Soc. 2018, 140, 18115–18123

boundaries. We note that the trace amount of Se is not observed in the SPS-pressed samples used for property measurements, as described below. Collectively, the absorption and XRD data indicate that the bandgap of PbSe increases with the incorporation of Hg and the solubility limit is approximately 6%.

The blueshift in the bandgap of PbSe-$x$%HgSe is somewhat unexpected, since HgSe itself is a semimetal ($E_g$ = 0). We attribute this unexpected behavior to the fact that $Hg^{2+}$ is in an unusual coordination environment when alloyed into PbSe (nominally octahedral), whereas in zincblende-type HgSe it is found in the tetrahedral sites. We note that Hg is rarely found with true octahedral coordination in either solids or molecules, and this observation led us to speculate that the $Hg^{2+}$ cations may sit at an off-centered position within the Se sublattice. Local breaking of symmetry can allow orbital hybridization that would otherwise be forbidden, yielding stronger bonding interactions that lower the energy of the system.[38,39] Such off-centering is being observed with increasing frequency and can lead to emergent properties.[40,41] For example, dynamic off-centering in hybrid halide perovskites has been shown to facilitate greater polarizability in these materials, which helps to explain their remarkable defect-tolerant transport properties.[42,43] Importantly, off-centering phenomena are often not detected using bulk diffraction, since these methods rely on the statistical average of atomic positions and do not perceive local, random distortions.

To probe the local structural environment of Hg and Se within the PbSe−6%HgSe sample, we employed $^{199}$Hg and $^{77}$Se NMR. Solid-state NMR has emerged as a powerful technique for probing the coordination environment of transition metals in solids and provides information regarding subtle distortions within a given coordination geometry.[44] The $^{199}$Hg CPMG static NMR spectra together with the corresponding spectral simulations are shown in Figure 3a, and parameters used for the simulations are shown in Table S1. The $^{199}$Hg NMR spectrum of HgSe exhibits two components, and the major one resonates at −1642 ppm with a shift anisotropy of 27 ppm that is assigned to Hg with tetrahedral coordination. The resonance position is greatly displaced from 0 ppm due to interactions between Hg and charge carriers (the so-called Knight shift), while the shift anisotropy strongly depends on the symmetry of the local structural environment.[45] The highly symmetric tetrahedral coordination renders the shift anisotropy very small, 27 ppm. The second minor component of the $^{199}$Hg NMR spectrum of HgSe has a resonance position of −1720 ppm with a shift anisotropy of 200 ppm. Based on previous investigations on mercury complexes, the large anisotropy parameter indicates a linear coordination environment for Hg.[46] This may be due to a trace amount of the cinnabar-type HgSe (which has Hg in a linear coordination). The $^{199}$Hg NMR spectrum of PbSe−6%HgSe shows one component with a shift of −1860 ppm and a shift anisotropy of 65 ppm. We attribute the difference in $^{199}$Hg shifts for HgSe and PbSe-6%HgSe to the different coordination environments in the two systems. Importantly, the increased shift anisotropy of Hg in PbSe−6%HgSe compared to HgSe indicates a less symmetric environment,[44] likely a distorted position. The $^{77}$Se NMR spectrum of HgSe, which is shown in Figure 3b, displays one single sharp resonance at −245 ppm with a very small shift anisotropy of 2.4 ppm, while the $^{77}$Se NMR spectrum of PbSe−6%HgSe shows a resonance at −710 ppm with a shift anisotropy of 46 ppm. Again, the relatively

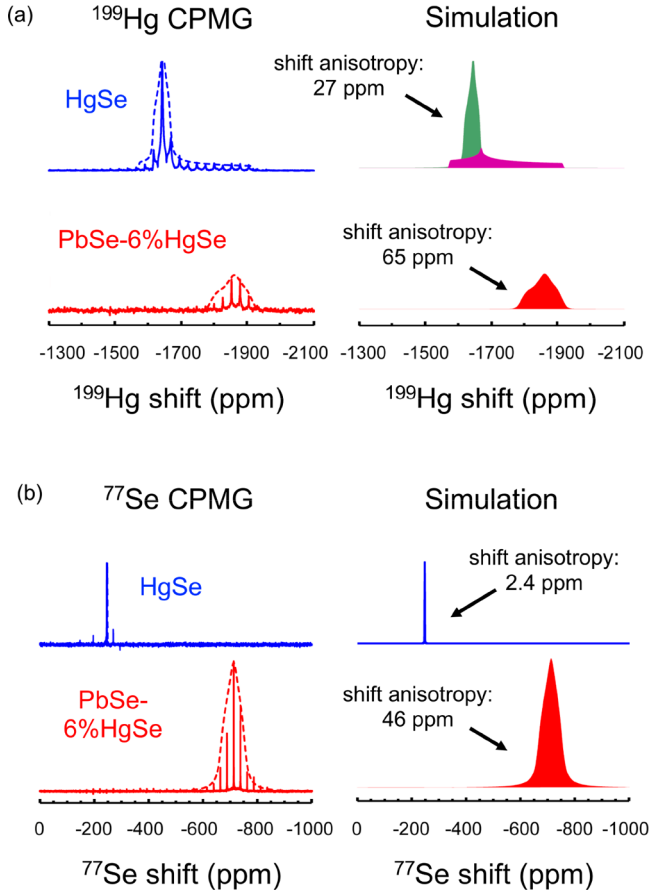


**Figure 3.** (a) $^{199}$Hg CPMG static NMR spectra together with the corresponding spectral simulations for HgSe and PbSe−6%HgSe. The major peak (green) in the HgSe spectrum is attributed to Hg at the tetrahedral site within HgSe, and the small shift anisotropy (27 ppm) indicates high symmetry. Conversely, the PbSe−6%HgSe spectrum (red) shows a large shift anisotropy of 65 ppm, indicating an asymmetric bonding environment. (b) $^{77}$Se CPMG static NMR spectra together with the corresponding spectral simulations for HgSe and PbSe−6%HgSe. The small shift anisotropy (2.4 ppm) observed in the HgSe sample is expected with the high symmetry coordination environment for Hg (tetrahedral), whereas the greater 46 ppm value for the PbSe−6%HgSe sample indicates a lower symmetry, off-centered position.

large $^{77}$Se shift anisotropy is an indication of a less symmetric structural environment for Se in $Pb_{0.94}Hg_{0.06}Se$ compared with that in HgSe. Taken together, the NMR data suggest that Hg does not sit at the center of the octahedral position within the PbSe matrix, which is consistent with its well-known chemical tendency to avoid this type of coordination geometry.[30] The nature of the off-centering and its influence on thermal transport are discussed in detail below.

To determine the p-type properties of Hg-alloyed PbSe, a series of Na-doped samples with the composition $Pb_{0.98}Na_{0.02}Se$−$x$%HgSe ($x$ = 0−5) were synthesized using the high-temperature methods described above. The resulting ingots (Figure S3) were ground and passed through a 100 $\mu$m sieve, followed by spark plasma sintering. The densified pellets were then cut and polished into the appropriate sizes and shapes for transport measurements. A representative pellet is shown in Figure S3, and all the samples were found to have densities greater than 95% of the theoretical value. SEM and EBSD for the $Pb_{0.98}Na_{0.02}Se$−$x$%HgSe pellet are shown in


DOI: 10.1021/jacs.8b11050
J. Am. Chem. Soc. 2018, 140, 18115−18123

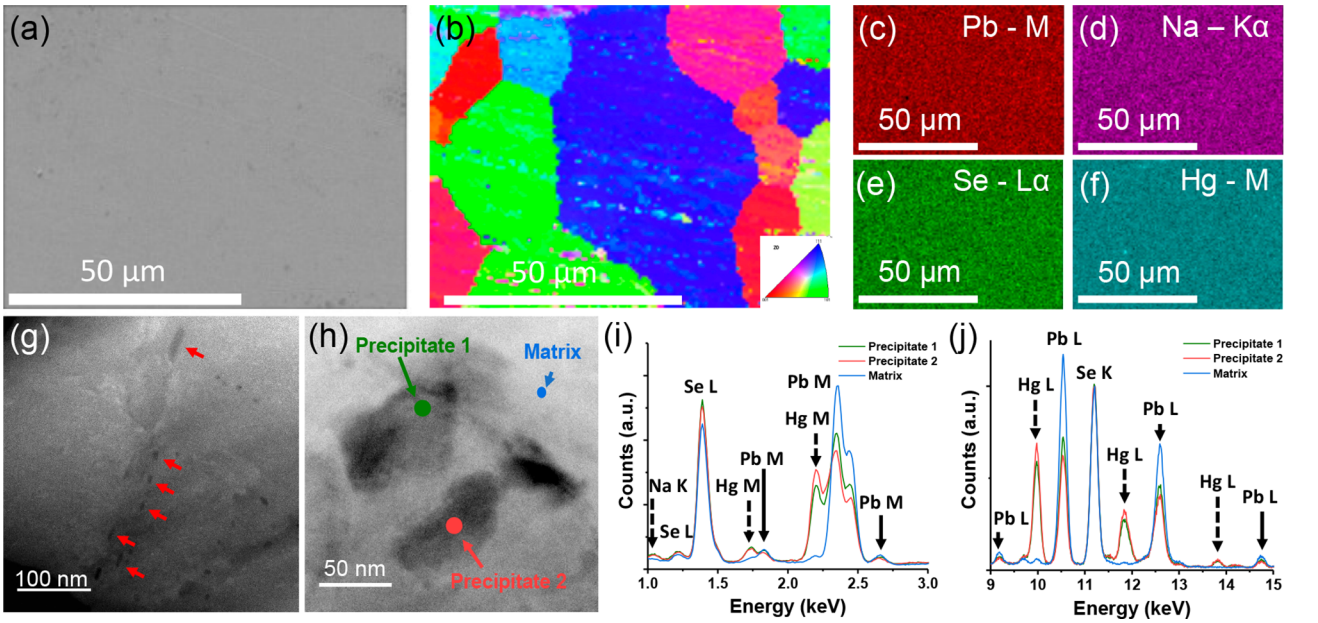


**Figure 4.** Analytical electron microscopy for $Pb_{0.98}Na_{0.02}Se-2\%HgSe$. (a) Secondary electron image of the sample surface that was characterized using both (b) EBSD and (c–f) SEM-EDS. The SEM data reveals distinct grains with no meaningful chemical segregation detected at the micrometer length scale. (g and h) HAADF STEM images of $Pb_{0.98}Na_{0.02}Se-2\%HgSe$. Point EDS spectra were obtained at the three locations (green, red, and blue dots) indicated in part h. (i and j) Three spectra shown in the energy range of 1–3 and 9–15 keV, respectively. The three spectra obtained from precipitates 1 and 2 and the matrix were normalized using the Se K peak.

Figure 4a and b, respectively, along with the corresponding EDS maps (4c–f), which show distinct grain boundaries in the samples but no chemical segregation at the micrometer scale. Figure 4g and h show high magnification HAADF-STEM images of the sample and reveal nanoscale precipitates in the matrix. The composition of the precipitates was characterized with EDS. Point EDS spectra were obtained from two different precipitates, and the locations are indicated with green and red dots, as shown in Figure 4h. An additional EDS spectrum was obtained from the matrix as located by the blue dot. In order to compare the chemical composition of the spots, the three spectra were normalized using the Se K peak. The 1–3 keV energy range and 9–15 keV energy range of the same three spectra are shown in Figure 4i and j, respectively. The EDS analysis shows that the precipitates are rich in Hg and deficient in Pb, compared to the surrounding matrix. The presence of Hg precipitates in the $Pb_{0.98}Na_{0.02}Se-x\%HgSe$ pellet suggests that the incorporation of Na may decrease the solubility of Hg in PbSe.

Figure 5 shows the temperature-dependent electronic transport properties for the various $Pb_{0.98}Na_{0.02}Se-x\%HgSe$ samples. As expected, the electrical conductivity decreases with increasing temperature due to carrier-phonon scattering and is consistent with degenerate semiconductor behavior (Figure 5a). The values range from 1500 to 2500 $S\cdot cm^{-1}$ at room temperature depending on the amount of Hg in the sample, and span 250–500 $S\cdot cm^{-1}$ at 900 K. At low temperatures there is a slight deviation from the expected $1/T$ behavior, which we believe is due to grain boundary scattering effects described by Kuo et al.[47] and is not observed in the temperature regime that is the focus of this study.

Figure 5b shows the temperature-dependent Seebeck coefficients, which are positive in all cases indicating p-type behavior. The room temperature values are approximately 25 $\mu V\cdot K^{-1}$ for all of the samples, but upon heating, the Hg-alloyed

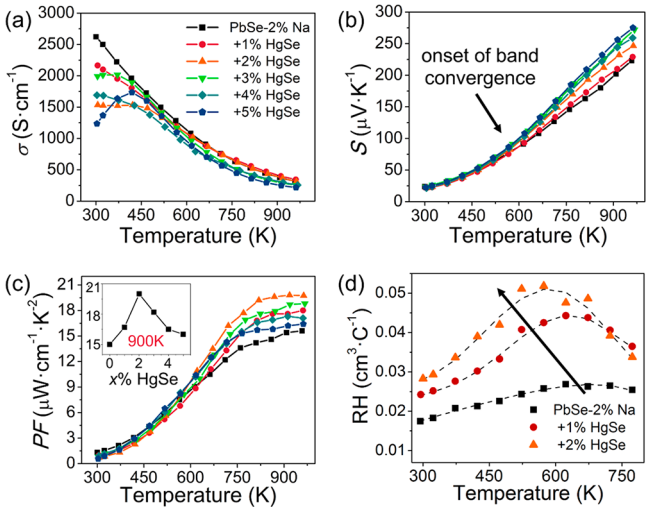


**Figure 5.** Electronic properties as a function of temperature for $Pb_{0.98}Na_{0.02}Se-x\%HgSe$. (a) Electrical conductivity, (b) Seebeck coefficient, and (c) power factor with inset showing values at 900 K for $x = 0-5$. (d) Temperature-dependent Hall data, showing a peak in the Hg-alloyed samples that shifts to lower temperature with increasing concentration.

samples show a marked enhancement beginning at approximately 550 K. The change in slope ultimately yields values exceeding 270 $\mu V\cdot K^{-1}$ at 962 K for 4% Hg, whereas the unalloyed $Pb_{0.98}Na_{0.02}Se$ sample is found to have value of 220 $\mu V\cdot K^{-1}$ at approximately the same temperature. Combined with the relatively high electrical conductivity, we find power factors as high as 20 $\mu W\cdot cm^{-1}\cdot K^{-2}$ in the $Pb_{0.98}Na_{0.02}Se-2\%$ HgSe sample. To the best of our knowledge, the highest value reported for p-type PbSe is 18 $\mu W\cdot cm^{-1}\cdot K^{-2}$ in the $Pb_{0.99}Na_{0.01}Se$-2%SrSe alloy,[48] and accordingly, the power factors reported here represent a new record.



DOI: 10.1021/jacs.8b11050
J. Am. Chem. Soc. 2018, 140, 18115–18123

Temperature-dependent Hall measurements were employed to probe the origin of the enhanced electronic properties. For semiconductors with charge carriers in a single band, the Hall coefficient ($R_H$) is expected to be temperature independent, while materials with two or more contributing bands will exhibit more complex behavior. Figure 5d shows temperature-dependent $R_H$ for the $Pb_{0.98}Na_{0.02}Se-x\%HgSe$ samples for $x$ = 0, 1, and 2. As expected, the $R_H$ values for the $x$ = 0 sample are nearly temperature independent, with a small peak at ~700 K. In contrast, the Hg-alloyed samples show noticeable peaks that clearly shift to lower temperature with increasing Hg content, providing strong evidence for contribution from multiple bands at the Fermi level. This is commonly observed in p-type PbTe systems and is attributed to the convergence of valence bands located at the L-point and along the $\sum$-line in the Brillouin zone, and typically occurs around 450−500 K.[22] Here, the highest performing $Pb_{0.98}Na_{0.02}Se-2\%HgSe$ sample shows a peak between 550 and 600 K, which is comparable to heavily doped PbTe. Supplementary Table 2 shows the room-temperature electronic transport properties of $Pb_{0.98}Na_{0.02}Se-x$%HgSe, along with data for the $Pb_{0.98}Na_{0.02}Se-x\%CdSe$ and $Pb_{0.98}Na_{0.02}Se-x\%ZnSe$ systems reported by Zhao et al.[14] Although having similar hole concentration ($N_p$), the carrier mobility ($\mu$) of the 2% HgSe sample (61 $cm^2 \cdot V^{-1} \cdot s^{-1}$) is found to be higher than that of 2% CdSe (37 $cm^2 \cdot V^{-1} \cdot s^{-1}$) and 2% ZnSe (36 $cm^2 \cdot V^{-1} \cdot s^{-1}$). We attribute the enhanced $\mu$ to the smaller radius contrast between $Pb^{2+}$ (1.29 Å) and $Hg^{2+}$ (1.02 Å) and similar degree of covalency of the M-Se bonds, which we believe results in a lower concentration of crystal defects and less scattering.[23] The relatively high $\mu$ combined with the band convergence now occurring at lower temperature in this system explains the high power factor observed in the Hg-alloyed PbSe system.

The thermal transport properties as a function of temperature were determined using the laser-flash diffusivity method, and the details of the measurement and pertinent calculations are provided in the Experimental Section. Figure 6a shows the total thermal conductivity ($\kappa_{tot}$) of the samples as a function of temperature (see Figure S4 for thermal diffusivity data). We observe that the room temperature thermal conductivity decreases with increasing amount of Hg, dropping from approximately 4.5 $W \cdot m^{-1} \cdot K^{-1}$ ($Pb_{0.98}Na_{0.02}Se$) to less than 4 $W \cdot m^{-1} \cdot K^{-1}$ for the $Pb_{0.98}Na_{0.02}Se-1\%HgSe$ sample, followed by a small but observable decrease thereafter. The $\kappa_{tot}$ values decrease with increasing temperature, as expected for degenerate semiconductors, and drops to approximately 1.1 $W \cdot m^{-1} \cdot K^{-1}$ at 950 K for the 5% Hg-alloyed sample. The lattice thermal conductivity ($\kappa_{lat}$) was determined by subtracting the electronic component ($\kappa_{elec}$) from the $\kappa_{tot}$ and exhibits a similar trend, as shown in Figure 6b. Specifically, for the high-performance $Pb_{0.98}Na_{0.02}Se-2\%HgSe$ composition, we see a value of 0.68 $W \cdot m^{-1} \cdot K^{-1}$ at ~950 K, which is noticeably lower than the unalloyed sample (~0.88 $W \cdot m^{-1} \cdot K^{-1}$), as well as other similar PbSe−2%MSe systems.[14,48] This is somewhat unexpected, since Hg and Pb have nearly identical atomic mass, and accordingly, Hg-alloying is not expected to produce significant mass fluctuation scattering to strongly affect thermal transport. Figure 6c shows the figure of merit $ZT$ of the samples as a function of temperature, showing a high $ZT$ of approximately 1.7 at 950 K in the $Pb_{0.98}Na_{0.02}Se-2\%HgSe$ sample, which is the highest value reported for p-type PbSe.

To better understand the nature of the asymmetric coordination environment of Hg in PbSe, and its effect on thermal transport, we used density functional theory (DFT) to calculate the total energy of the $Pb_{26}Se_{27}Hg_1$ supercell (see Supporting Information for experimental details) with Hg located at various positions between the octahedral and tetrahedral sites (Figure 7a). We observe that the system has an energetic minimum when Hg is approximately 0.2 Å away from the octahedral center, which suggests an off-centered position that corroborates the NMR data shown above. Critically, off-centered atoms, which we deem "discordant", can lower phonon velocities and introduce additional phonon scattering modes,[3,33,49,50] as well as alter the electronic properties of semiconductors.[51] We also calculated $\kappa_{lat}$ using DFT for pure PbSe and PbSe−1.5%HgSe with Hg in the off-centered position. By comparing the phonon dispersions of the two systems (Figure S5), we find that the longitudinal Debye temperature and phonon velocity is lower in Hg-Alloyed PbSe than in pure PbSe. Specifically, the average longitudinal Debye temperature is calculated to be 65 K for pure PbSe and 44 K

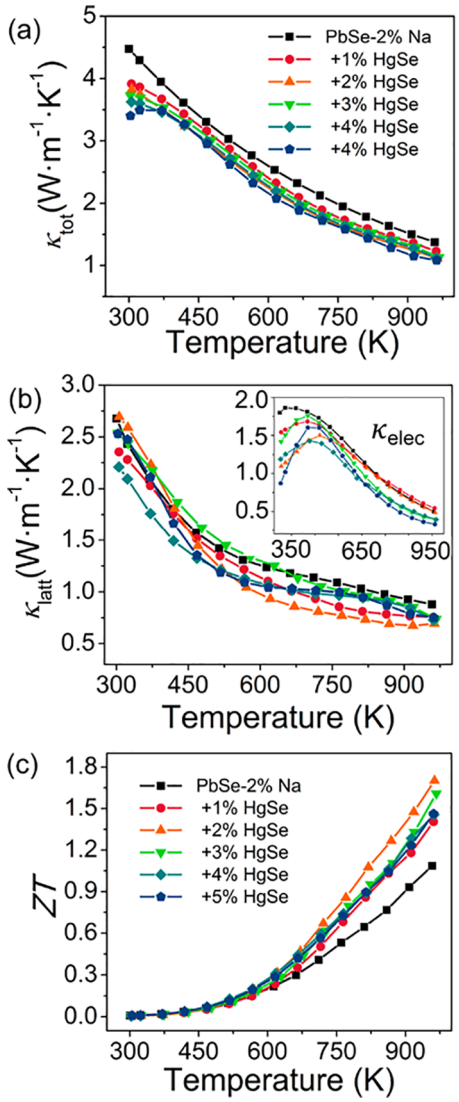


**Figure 6.** (a) Total thermal conductivity and (b) lattice thermal conductivity of the PbSe−$x$%HgSe samples as a function of temperature, with the electronic component shown in the inset. (c) Figure of merit $ZT$ as a function of temperature for the PbSe−$x$% HgSe samples, showing a peak value of approximately 1.7 for the $x$ = 2 sample at 950 K.



DOI: 10.1021/jacs.8b11050
J. Am. Chem. Soc. 2018, 140, 18115−18123

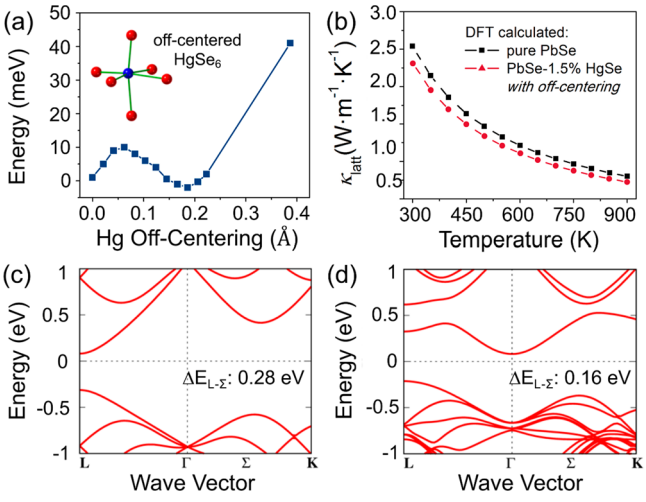


**Figure 7.** (a) Plot showing the total energy of PbSe−4%HgSe with Hg placed at various positions between the octahedral and tetrahedral sites, showing local minima at approximately 0.2 Å from the octahedral center. (b) DFT-calculated $\kappa_{lat}$ for PbSe and PbSe-1.5% HgSe with off-centered Hg cation. (c) DFT-calculated band structures for pure PbSe and (d) PbSe-4%HgSe, indicating that Hg-alloying decreases the energy offset between the L-band and $\sum$-band.

for PbSe−1.5%HgSe, while the average phonon velocity of pure PbSe is 2614 and 2550 $ms^{-1}$ for PbSe−1.5%HgSe. The calculated $\kappa_{lat}$ for the two systems is shown in Figure 7b, displaying room-temperature values of 2.5 and 2.3 $W{\cdot}m^{-1}{\cdot}K^{-1}$ for PbSe and PbSe−1.5%HgSe, respectively. This data strongly suggests that the discordant Hg atoms play a role in suppressing thermal conductivity, although it is difficult to quantitatively determine its true contribution due to the presence of Hg-rich nanoprecipitates, which can also act as phonon scattering centers.

The effect of Hg-alloyed into PbSe on the electronic structure, was probed with first-principles density functional theory (DFT) electronic structure calculations using the $Pb_{27}Se_{27}$ (pure PbSe) and $Pb_{26}Se_{27}Hg_1$ (PbSe-4%HgSe) supercell with the off-centered Hg position (experimental details can be found in the Supporting Information). The DFT band structure with spin−orbit coupling for pure PbSe is shown in Figure 7c, and the band structure for PbSe−4%HgSe is shown in Figure 7d. The electronic structure for pure PbSe shows a primary valence band at the L-point and heavy secondary band along the $\sum$-line, with a band offset of 0.28 eV, which is consistent with previous studies. It is apparent from Figure 7d that there is an impurity state in the conduction band of the Hg-alloyed band structure, which runs up from the Γ-point to the L-point. The direct gap at the L-point is found to increase relative to pure PbSe, which is consistent with the FTIR data. Importantly, the energy offset between the L-band and lower lying $\sum$-band ($\Delta E_{L\text{-}\sum}$) is found to decrease significantly from 0.28 eV (pure PbSe) to 0.16 eV in PbSe-4%HgSe. It is known that in PbQ (Q = S, Se, Te) as the temperature increases the valence band (L-point) decreases in energy, until at some critical temperature it converges with the lower lying $\sum$-band.[51−54] Since the L-band and $\sum$-band have 4-fold and 12-fold valley degeneracy ($N_v$), respectively, this convergence results in a combined 16-fold $N_v$.[2,23,27] This is important, since large band degeneracy yields an increase in the density of states and greater carrier entropy, which delivers a large boost to the thermopower.[2,22,27,55]

Accordingly, the decrease in $\Delta E_{L\text{-}\sum}$ for $Pb_{1-x}Hg_xSe$ is expected to lower the temperature at which band convergence occurs, and also provide a boost to the thermopower, which is consistent with the temperature-dependent Hall measurements described above. Taking all of the data into consideration, we attribute the augmented electronic properties to the early onset of band convergence, which is facilitated by a decrease in $\Delta E_{L\text{-}\sum}$ in the Hg-alloyed samples.

## CONCLUSIONS

The new $Pb_{0.98\text{-}x}Na_{0.02}$−x%HgSe system we presented above achieves a power factor of 20 $\mu W{\cdot}cm^{-1}{\cdot}K^{-2}$ at 950 K, which outperforms any other p-type PbSe system to date and delivers a record high figure of merit $ZT$ of 1.7. The enhancement reflects the sharp increase in the slope of $S$ at around 550 K, attributed to the early onset of valence band convergence. In general, it is much more challenging to increase the power factor in top thermoelectric materials than to decrease thermal conductivity. Unlike in previous reports where increases in $ZT$ for PbSe were achieved with large decreases in thermal conductivity, in the present case we have shown how $ZT$ can be improved by increasing the power factor.

In addition to displaying outstanding thermoelectric performance, the PbSe−x%HgSe samples provide a model system for probing local asymmetry in lead chalcogenide alloys. Using $^{199}Hg$ and $^{77}Se$ NMR, we show evidence for Hg asymmetry within the PbSe lattice, which was anticipated because $Hg^{2+}$ is rarely found in true octahedral coordination. DFT calculations indicate that the Hg atoms are likely sitting approximately 0.2 Å away from the center of the octahedral site, and we dub the off-centered atoms "discordant", since they deviate from the periodicity of the PbSe matrix. It is likely that this distortion lowers the lattice thermal conductivity of the material. We believe this may be an important, yet overlooked aspect in lead chalcogenide thermoelectrics, which could inspire new criteria for designing high performance materials.

## ASSOCIATED CONTENT

### Supporting Information

The Supporting Information is available free of charge on the ACS Publications website at DOI: 10.1021/jacs.8b11050.

Indexed pXRD data for PbSe−10%HgSe; SEM and EBSD data for PbSe−6%HgSe; table containing NMR parameters used in simulations; experimental details for pXRD and electrical measurements, image of $Pb_{0.98-x}Na_{0.02}$−x%HgSe ingot and corresponding SPS-pressed pellet; temperature-dependent thermal diffusivity data for $Pb_{0.98-x}Na_{0.02}$−x%HgSe samples; DFT-calculated phonon dispersions for PbSe−1.5%HgSe and pure PbSe (PDF)

## AUTHOR INFORMATION

### Corresponding Author

*m-kanatzidis@northwestern.edu

### ORCID

Yan-Yan Hu: 0000-0003-0677-5897
Vinayak P. Dravid: 0000-0002-6007-3063
Chris Wolverton: 0000-0003-2248-474X
Mercouri G. Kanatzidis: 0000-0003-2037-4168



DOI: 10.1021/jacs.8b11050
J. Am. Chem. Soc. 2018, 140, 18115−18123

## Notes

The authors declare no competing financial interest.

## ■ ACKNOWLEDGMENTS

This research was funded primarily by U.S. Department of Energy, 587 Office of Science, and Office of Basic Energy Sciences under Award Number DE-SC-0014520. This work was partly supported (J.M.H.) by the Midwest Integrated Center for Computational Materials (MICCoM) as part of the Computational Materials Sciences Program funded by the U.S. Department of Energy, Office of Science, Basic Energy Sciences, Materials Sciences and Engineering Division (No. 5J-30161-0010A) (sample design, synthesis and characterization). This work made use of the EPIC facilities of Northwestern University's NUANCE Center, which has received support from the Soft and Hybrid Nanotechnology Experimental (SHyNE) Resource (NSF ECCS-1542205); the MRSEC program (NSF DMR-1720139) at the Materials Research Center; the International Institute for Nanotechnology (IIN); the Keck Foundation; and the State of Illinois, through the IIN. User facilities are supported by the Office of Science of the U.S. Department of Energy under contract No. DE-AC02-06CH11357 and DE-AC02-05CH11231. Access to facilities of high performance computational resources at the Northwestern University is acknowledged. JAG acknowledges support from the National Science Foundation Graduate Research Fellowship under Grant No. DGE-1324585.

## ■ REFERENCES

(1) Lewis, N. S.; Nocera, D. G. Powering the Planet: Chemical Challenges in Solar Energy Utilization. *Proc. Natl. Acad. Sci. U. S. A.* **2006**, *103* (43), 15729−15735.

(2) Tan, G.; Zhao, L.-D.; Kanatzidis, M. G. Rationally Designing High-Performance Bulk Thermoelectric Materials. *Chem. Rev.* **2016**, *116* (19), 12123−12149.

(3) Snyder, G. J.; Toberer, E. S. Complex Thermoelectric Materials. *Nat. Mater.* **2008**, *7* (2), 105−114.

(4) Poudel, B.; Hao, Q.; Ma, Y.; Lan, Y.; Minnich, A.; Yu, B.; Yan, X.; Wang, D.; Muto, A.; Vashaee, D.; Chen, X.; Liu, J.; Dresselhaus, M. S.; Chen, G.; Ren, Z. High-Thermoelectric Performance of Nanostructured Bismuth Antimony Telluride Bulk Alloys. *Science* **2008**, *320* (5876), 634−638.

(5) Sootsman, J. R.; Chung, D. Y.; Kanatzidis, M. G. New and Old Concepts in Thermoelectric Materials. *Angew. Chem., Int. Ed.* **2009**, *48* (46), 8616−8639.

(6) Zhao, L.-D.; Lo, S.-H.; Zhang, Y.; Sun, H.; Tan, G.; Uher, C.; Wolverton, C.; Dravid, V. P.; Kanatzidis, M. G. Ultralow Thermal Conductivity and High Thermoelectric Figure of Merit in SnSe Crystals. *Nature* **2014**, *508* (7496), 373−377.

(7) Zhao, L.-D.; Tan, G.; Hao, S.; He, J.; Pei, Y.; Chi, H.; Wang, H.; Gong, S.; Xu, H.; Dravid, V. P.; Uher, C.; Snyder, G. J.; Wolverton, C.; Kanatzidis, M. G. Ultrahigh Power Factor and Thermoelectric Performance in Hole-Doped Single-Crystal SnSe. *Science* **2016**, *351* (6269), 141−144.

(8) Chang, C.; Wu, M.; He, D.; Pei, Y.; Wu, C.-F.; Wu, X.; Yu, H.; Zhu, F.; Wang, K.; Chen, Y.; Huang, L.; Li, J.-F.; He, J.; Zhao, L.-D. 3D Charge and 2D Phonon Transports Leading to High Out-of-Plane ZT in n-Type SnSe Crystals. *Science* **2018**, *360* (6390), 778−783.

(9) Lalonde, A. D.; Pei, Y.; Wang, H.; Jeffrey Snyder, G. Lead Telluride Alloy Thermoelectrics. *Mater. Today* **2011**, *14* (11), 526−532.

(10) Wang, H.; Pei, Y.; LaLonde, A. D.; Snyder, G. J. Heavily Doped P-Type PbSe with High Thermoelectric Performance: An Alternative for PbTe. *Adv. Mater.* **2011**, *23* (11), 1366−1370.

(11) Li, G.; Aydemir, U.; Duan, B.; Agne, M. T.; Wang, H.; Wood, M.; Zhang, Q.; Zhai, P.; Goddard, W. A.; Snyder, G. J. Micro-and Macromechanical Properties of Thermoelectric Lead Chalcogenides. *ACS Appl. Mater. Interfaces* **2017**, *9* (46), 40488−40496.

(12) Zhang, X.; Zhao, L.-D. Thermoelectric Materials: Energy Conversion between Heat and Electricity. *J. Mater.* **2015**, *1* (2), 92−105.

(13) Parker, D.; Singh, D. J. High-Temperature Thermoelectric Performance of Heavily Doped PbSe. *Phys. Rev. B: Condens. Matter Mater. Phys.* **2010**, *82* (3), 035204.

(14) Zhao, L.-D.; Hao, S.; Lo, S.-H.; Wu, C.-I.; Zhou, X.; Lee, Y.; Li, H.; Biswas, K.; Hogan, T. P.; Uher, C.; Wolverton, C.; Dravid, V. P.; Kanatzidis, M. G. High Thermoelectric Performance via Hierarchical Compositionally Alloyed Nanostructures. *J. Am. Chem. Soc.* **2013**, *135* (19), 7364−7370.

(15) Kanatzidis, M. G. Nanostructured Thermoelectrics: The New Paradigm? *Chem. Mater.* **2010**, *22* (3), 648−659.

(16) Hu, L.; Zhu, T.; Liu, X.; Zhao, X. Point Defect Engineering of High-Performance Bismuth-Telluride-Based Thermoelectric Materials. *Adv. Funct. Mater.* **2014**, *24* (33), 5211−5218.

(17) Zhao, L.-D.; Dravid, V. P.; Kanatzidis, M. G. The Panoscopic Approach to High Performance Thermoelectrics. *Energy Environ. Sci.* **2014**, *7* (1), 251−268.

(18) Vineis, C. J.; Shakouri, A.; Majumdar, A.; Kanatzidis, M. G. Nanostructured Thermoelectrics: Big Efficiency Gains from Small Features. *Adv. Mater.* **2010**, *22* (36), 3970−3980.

(19) Zhou, C.; Yu, Y.; Lee, Y. K.; Cojocaru-Mirédin, O.; Yoo, B.; Cho, S.-P.; Im, J.; Wuttig, M.; Hyeon, T.; Chung, I. High-Performance n-Type PbSe−$Cu_2Se$ Thermoelectrics through Conduction Band Engineering and Phonon Softening. *J. Am. Chem. Soc.* **2018**, *140*, 15535.

(20) Tan, G.; Liu, W.; Wang, S.; Yan, Y.; Li, H.; Tang, X.; Uher, C. Rapid Preparation of $CeFe_4Sb_{12}$ Skutterudite by Melt Spinning: Rich Nanostructures and High Thermoelectric Performance. *J. Mater. Chem. A* **2013**, *1* (40), 12657−12668.

(21) Tan, G.; Chi, H.; Liu, W.; Zheng, Y.; Tang, X.; He, J.; Uher, C. Toward High Thermoelectric Performance P-Type $FeSb_{2.2}Te_{0.8}$ via in Situ Formation of InSb Nanoinclusions. *J. Mater. Chem. C* **2015**, *3* (32), 8372−8380.

(22) Pei, Y.; Shi, X.; LaLonde, A.; Wang, H.; Chen, L.; Snyder, G. J. Convergence of Electronic Bands for High Performance Bulk Thermoelectrics. *Nature* **2011**, *473* (7345), 66−69.

(23) Tan, G.; Shi, F.; Hao, S.; Zhao, L.-D.; Chi, H.; Zhang, X.; Uher, C.; Wolverton, C.; Dravid, V. P.; Kanatzidis, M. G. Non-Equilibrium Processing Leads to Record High Thermoelectric Figure of Merit in PbTe−SrTe. *Nat. Commun.* **2016**, *7*, 12167.

(24) Wang, H.; Gibbs, Z. M.; Takagiwa, Y.; Snyder, G. J. Tuning Bands of PbSe for Better Thermoelectric Efficiency. *Energy Environ. Sci.* **2014**, *7* (2), 804−811.

(25) Pei, Y.; Chang, C.; Wang, Z.; Yin, M.; Wu, M.; Tan, G.; Wu, H.; Chen, Y.; Zheng, L.; Gong, S.; Zhu, T.; Zhao, X.; Huang, L.; He, J.; Kanatzidis, M. G.; Zhao, L.-D. Multiple Converged Conduction Bands in $K_2Bi_8Se_{13}$: A Promising Thermoelectric Material with Extremely Low Thermal Conductivity. *J. Am. Chem. Soc.* **2016**, *138* (50), 16364−16371.

(26) Hanus, R.; Guo, X.; Tang, Y.; Li, G.; Snyder, G. J.; Zeier, W. G. A Chemical Understanding of the Band Convergence in Thermoelectric $CoSb_3$ Skutterudites: Influence of Electron Population, Local Thermal Expansion, and Bonding Interactions. *Chem. Mater.* **2017**, *29* (3), 1156−1164.

(27) Tang, Y.; Gibbs, Z. M.; Agapito, L. A.; Li, G.; Kim, H.-S.; Nardelli, M. B.; Curtarolo, S.; Snyder, G. J. Convergence of Multi-Valley Bands as the Electronic Origin of High Thermoelectric Performance in $CoSb_3$ Skutterudites. *Nat. Mater.* **2015**, *14* (12), 1223−1228.

(28) Zhao, L. D.; Wu, H. J.; Hao, S. Q.; Wu, C. I.; Zhou, X. Y.; Biswas, K.; He, J. Q.; Hogan, T. P.; Uher, C.; Wolverton, C.; Dravid, V. P.; Kanatzidis, M. G. All-Scale Hierarchical Thermoelectrics: MgTe in PbTe Facilitates Valence Band Convergence and Suppresses Bipolar Thermal Transport for High Performance. *Energy Environ. Sci.* **2013**, *6* (11), 3346.



DOI: 10.1021/jacs.8b11050
*J. Am. Chem. Soc.* 2018, 140, 18115−18123

(29) Pei, Y.; Wang, H.; Snyder, G. J. Band Engineering of Thermoelectric Materials. *Adv. Mater.* **2012**, *24* (46), 6125−6135.
(30) Levason, W.; McAuliffe, C. A. The Coordination Chemistry of Mercury. In *The Chemistry of Mercury*; Palgrave Macmillan UK: London, 1977; pp 47−135.
(31) Nilsson, K. B.; Maliarik, M.; Persson, I.; Fischer, A.; Ullström, A.-S.; Eriksson, L.; Sandström, M. Coordination Chemistry of Mercury(II) in Liquid and Aqueous Ammonia Solution and the Crystal Structure of Tetraamminemercury(II) Perchlorate. *Inorg. Chem.* **2008**, *47* (6), 1953−1964.
(32) Bersuker, I. B. Modern Aspects of the Jahn−Teller Effect Theory and Applications To Molecular Problems. *Chem. Rev.* **2001**, *101*, 1067.
(33) Luo, Z.-Z.; Hao, S.; Zhang, X.; Hua, X.; Cai, S.; Tan, G.; Bailey, T. P.; Ma, R.; Uher, C.; Wolverton, C.; Dravid, V. P.; Yan, Q.; Kanatzidis, M. G. Soft Phonon Modes from Off-Center Ge Atoms Lead to Ultralow Thermal Conductivity and Superior Thermoelectric Performance in n-Type PbSe−GeSe. *Energy Environ. Sci.* **2018**, *11*, 3220.
(34) Axtell, E. A.; Liao, J.-H.; Pikramenou, Z.; Kanatzidis, M. G. Dimensional Reduction in II-VI Materials: $A_2Cd_3Q_4$ (A = K, Q = S, Se, Te; A = Rb, Q = S, Se), Novel Ternary Low-Dimensional Cadmium Chalcogenides Produced by Incorporation of $A_2Q$ in CdQ. *Chem. - Eur. J.* **1996**, *2* (6), 656−666.
(35) Hung, I.; Rossini, A. J.; Schurko, R. W. Application of the Carr−Purcell Meiboom−Gill Pulse Sequence for the Acquisition of Solid-State NMR Spectra of Spin-1/2 Nuclei. *J. Phys. Chem. A* **2004**, *108*, 7112.
(36) Harris, R. K.; Becker, E. D.; Cabral de Menezes, S. M.; Goodfellow, R.; Granger, P. NMR Nomenclature: Nuclear Spin Properties and Conventions for Chemical Shifts: IUPAC Recommendations 2001. *Solid State Nucl. Magn. Reson.* **2002**, *22* (4), 458−483.
(37) Lee, Y.; Lo, S.-H.; Chen, C.; Sun, H.; Chung, D.-Y.; Chasapis, T. C.; Uher, C.; Dravid, V. P.; Kanatzidis, M. G. Contrasting Role of Antimony and Bismuth Dopants on the Thermoelectric Performance of Lead Selenide. *Nat. Commun.* **2014**, *5*, 3640.
(38) Bersuker, I. B. Pseudo-Jahn−Teller Effect—A Two-State Paradigm in Formation, Deformation, and Transformation of Molecular Systems and Solids. *Chem. Rev.* **2013**, *113* (3), 1351−1390.
(39) Walsh, A.; Payne, D. J.; Egdell, R. G.; Watson, G. W. Stereochemistry of Post-Transition Metal Oxides: Revision of the Classical Lone Pair Model Stereochemistry of Post-Transition Metal Oxides: Revision of the Classical Lone Pair Model. *Chem. Soc. Rev.* **2011**, *40* (40), 4455−4876.
(40) Božin, E. S.; Malliakas, C. D.; Souvatzis, P.; Proffen, T.; Spaldin, N. A.; Kanatzidis, M. G.; Billinge, S. J. L. Entropically Stabilized Local Dipole Formation in Lead Chalcogenides. *Science* **2010**, *330* (6011), 1660−1663.
(41) Knox, K. R.; Bozin, E. S.; Malliakas, C. D.; Kanatzidis, M. G.; Billinge, S. J. L. Local Off-Centering Symmetry Breaking in the High-Temperature Regime of SnTe. *Phys. Rev. B: Condens. Matter Mater. Phys.* **2014**, *89* (1), 014102.
(42) Laurita, G.; Fabini, D. H.; Stoumpos, C. C.; Kanatzidis, M. G.; Seshadri, R. Chemical Tuning of Dynamic Cation Off-Centering in the Cubic Phases of Hybrid Tin and Lead Halide Perovskites. *Chem. Sci.* **2017**, *8* (8), 5628−5635.
(43) Fabini, D. H.; Laurita, G.; Bechtel, J. S.; Stoumpos, C. C.; Evans, H. A.; Kontos, A. G.; Raptis, Y. S.; Falaras, P.; Van der Ven, A.; Kanatzidis, M. G.; Seshadri, R. Dynamic Stereochemical Activity of the $Sn^{2+}$ Lone Pair in Perovskite $CsSnBr_3$. *J. Am. Chem. Soc.* **2016**, *138* (36), 11820−11832.
(44) Natan, M. J.; Millikan, C. F.; Wright, J. G.; O'Halloran, T. V. Solid-State Mercury-199 Nuclear Magnetic Resonance as a Probe of Coordination Number and Geometry in Hg(II) Complexes. *J. Am. Chem. Soc.* **1990**, *112* (8), 3255−3257.
(45) Laws, D. D.; Bitter, H.-M. L.; Jerschow, A. Solid-State NMR Spectroscopic Methods in Chemistry. *Angew. Chem., Int. Ed.* **2002**, *41* (17), 3096−3129.
(46) Bowmaker, G. A.; Churakov, A. V.; Harris, R. K.; Howard, J. A. K.; Apperley, D. C. Solid-State 199Hg MAS NMR Studies of Mercury(II) Thiocyanate Complexes and Related Compounds. Crystal Structure of Hg(SeCN)2. *Inorg. Chem.* **1998**, *37*, 1734.
(47) Kuo, J. J.; Kang, S. D.; Imasato, K.; Tamaki, H.; Ohno, S.; Kanno, T.; Snyder, G. J. Grain Boundary Dominated Charge Transport in $Mg_3Sb_2$ -Based Compounds. *Energy Environ. Sci.* **2018**, *11* (2), 429−434.
(48) Lee, Y.; Lo, S.-H.; Androulakis, J.; Wu, C.-I.; Zhao, L.-D.; Chung, D.-Y.; Hogan, T. P.; Dravid, V. P.; Kanatzidis, M. G. High-Performance Tellurium-Free Thermoelectrics: All-Scale Hierarchical Structuring of p-Type PbSe−MSe Systems (M = Ca, Sr, Ba). *J. Am. Chem. Soc.* **2013**, *135* (13), 5152−5160.
(49) Toberer, E. S.; Zevalkink, A.; Snyder, G. J. Phonon Engineering through Crystal Chemistry. *J. Mater. Chem.* **2011**, *21* (40), 15843.
(50) Takasu, Y.; Hasegawa, T.; Ogita, N.; Udagawa, M.; Avila, M. A.; Suekuni, K.; Takabatake, T. Off-Center Rattling and Cage Vibration of the Carrier-Tuned Type-I Clathrate $Ba_8Ga_{16}Ge_{30}$ Studied by Raman Scattering. *Phys. Rev. B: Condens. Matter Mater. Phys.* **2010**, *82* (13), 134302.
(51) Zeier, W. G.; Zevalkink, A.; Gibbs, Z. M.; Hautier, G.; Kanatzidis, M. G.; Snyder, G. J. Thinking Like a Chemist: Intuition in Thermoelectric Materials. *Angew. Chem., Int. Ed.* **2016**, *55* (24), 6826−6841.
(52) Gibbs, Z. M.; Kim, H.; Wang, H.; White, R. L.; Drymiotis, F.; Kaviany, M.; Jeffrey Snyder, G. Temperature Dependent Band Gap in PbX (X = S, Se, Te). *Appl. Phys. Lett.* **2013**, *103* (26), 262109.
(53) Gibbs, Z. M.; LaLonde, A.; Snyder, G. J. Optical Band Gap and the Burstein−Moss Effect in Iodine Doped PbTe Using Diffuse Reflectance Infrared Fourier Transform Spectroscopy. *New J. Phys.* **2013**, *15* (7), 075020.
(54) Chasapis, T. C.; Lee, Y.; Hatzikraniotis, E.; Paraskevopoulos, K. M.; Chi, H.; Uher, C.; Kanatzidis, M. G. Understanding the Role and Interplay of Heavy-Hole and Light-Hole Valence Bands in the Thermoelectric Properties of PbSe. *Phys. Rev. B: Condens. Matter Mater. Phys.* **2015**, *91* (8), 085207.
(55) Wang, C. W.; Xia, Y. Y. Y.; Tian, Z.; Jiang, J.; Li, B. H.; Cui, S. T.; Yang, H. F.; Liang, A. J.; Zhan, X. Y.; Hong, G. H.; Liu, S.; Chen, C.; Wang, M. X.; Yang, L. X.; Liu, Z.; Mi, Q. M.; Li, G.; Xue, J. M.; Liu, Z. K.; Chen, Y. L. Photoemission Study of the Electronic Structure of Valence Band Convergent SnSe. *Phys. Rev. B: Condens. Matter Mater. Phys.* **2017**, DOI: 10.1103/PhysRevB.96.165118.


DOI: 10.1021/jacs.8b11050
*J. Am. Chem. Soc.* 2018, 140, 18115−18123